

Twist-bend nematic drops as colloidal particles: Electric instabilitiesK. S. Krishnamurthy^{1,*}, D. S. Shankar Rao,¹ Santosh Y. Khatavi,¹ and Channabasaveshwar V. Yelamagad^{1,2}¹Centre for Nano and Soft Matter Sciences, Survey No. 7, Shivanapura, Bangalore 562162, India²Manipal Academy of Higher Education, Madhav Nagar, Manipal 576104, India

(Received 19 January 2023; accepted 10 April 2023; published 28 April 2023)

The mesogen 1,7''-bis(4-cyanobiphenyl-4'-yl)heptane (CB7CB), doped with a small quantity of an amphiphilic compound, is examined in its biphasic state in which twist-bend nematic (N_{TB}) drops are dispersed in the isotropic fluid. Various flexoelectric and electrokinetic responses of small drops in their escaped-radial-like (ER) geometry, and also of larger ones with parabolic focal conic defects, are discussed. A pair of confocal parabolas with their axes along the applied low-frequency electric field undergo periodic dimensional changes so as to contribute flexoelectrically to free-energy reduction. In an ER droplet, the same result is achieved by periodic relocations of the hedgehog core. Sine-wave fields of low frequency and high voltage excite patterned states near zero-voltage crossings and homeotropic alignment at peak voltages. ER drops also exhibit electrohydrodynamic effects; in relatively weak fields, they undergo translatory motion with a velocity that is a quadratic in the field strength; the drift, which occurs over a very wide frequency range, extending from dc to MHz region, is enabled by radial symmetry breaking that their off-centered geometry entails; and the drift direction reverses across a critical frequency. In high fields, vortical flows occurring within an ER N_{TB} drop become discernible. The hydrodynamic effects are discussed based on the Taylor-Melcher leaky dielectric model.

DOI: [10.1103/PhysRevE.107.044703](https://doi.org/10.1103/PhysRevE.107.044703)**I. INTRODUCTION**

The twist-bend nematic (N_{TB}) phase, with its oblique helical molecular disposition and concomitantly winding polarization field, has been intensely investigated ever since its intriguing properties were brought to light by Panov *et al.* [1] and Cestari *et al.* [2]. Among its distinguishing properties are the particularly low bend modulus promoting the structural helicity [3–6], nanoscale pitch [7–10], spontaneously formed phase-grating modulation [1,11,12], electroclinic behavior [13–16], large flexoelectric coefficients [17], resemblance to layered systems [8,11,18–20] despite having no detectible density modulation [2,7,8], molecular unbending in magnetic fields [11,21], and a plethora of electric instabilities reviewed recently in Ref. [22]. In most studies of such properties, the N_{TB} phase is examined in its extended geometry. It has recently been found that the N_{TB} phase separating as droplets in the matrix of its own nematic or isotropic phase also possesses several notable structural and electro-optical features. The most intriguing of these is the growth pattern within radial N_{TB} drops, apparently involving expansion of the point +1 singularity into a closed constant torsion line disclination, with an approximate threefold symmetry [23]. More recent experiments on 1,7''-bis(4-cyanobiphenyl-4'-yl)heptane (CB7CB)-surfactant systems have revealed different flexoelectric responses in elastic dipoles [24], structural and electrokinetic features of *nematic* drops as colloidal particles [25], and Lehmann rotation of twisted bipolar *nematic* drops dis-

persed in the liquid [26]. In a continuing study, we have now examined the morphological features and electric instabilities of N_{TB} drops dispersed in the *isotropic* phase. The structure and stability aspects of the drops, in both nematic and isotropic environments, have already been discussed in our study [27]. In this paper, we deal with several notable electric-field effects relating to flexoelectric and electrohydrodynamic responses of the drops in the isotropic matrix. Among these effects are (a) field-induced periodic dimensional changes in a pair of confocal parabolae, (b) flexoelectric oscillations in escaped radial drops, (c) periodic formation in N_{TB} drops of patterned flexodielectric state in high fields, and (d) field-induced drift of escaped radial drops exhibited over a wide frequency region extending from dc to MHz. Our presentation of these results in Sec. III is supplemented by 12 movie clips, some optical microscopic textures, and connected notes, which are accessible in the Supplemental Material (SM) [28].

II. EXPERIMENT

The present studies concern binary mixtures of CB7CB with a surfactant, which is 2-octadecoxypropanol, OP, unless stated otherwise. These mixtures are referred as $C-OP_i$, with C for CB7CB and i for concentration in wt. % of the surfactant. With i in the range of 5–8, both the N and N_{TB} phases are observed to coexist with the isotropic over a few degrees Celsius, the onset of the N_{TB} phase occurring approximately in the range 89 °C to 94 °C in various mixtures; in the most commonly used mixtures, the $I-N$ and $N-N_{TB}$ onset temperatures T_N and T_{NTB} were $T_N = 99.0$ °C ($C-OP_5$), 94.7 °C ($C-OP_7$), and $T_{NTB} = 90.0$ °C ($C-OP_5$), 89.2 °C ($C-OP_7$). We used the following: for optical studies, a Carl-Zeiss

*Author to whom correspondence should be addressed: murthyksk@gmail.com

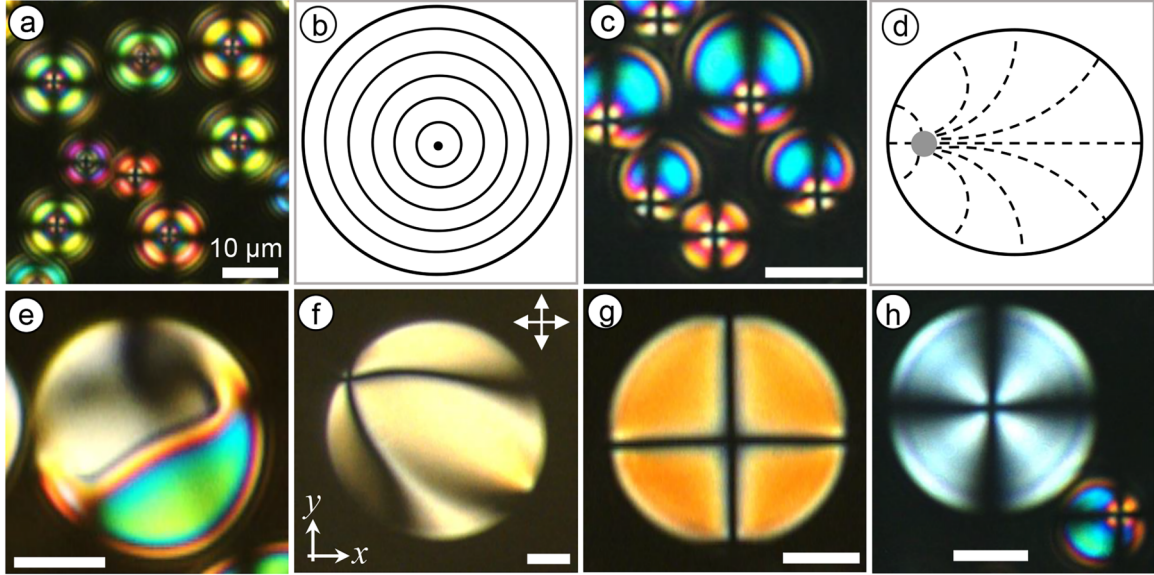


FIG. 1. N_{TB} droplets with varying director patterns, dispersed in the matrix of their isotropic phase. Smaller drops with diameter D below the sample thickness d are of radial hedgehog geometry (a), with their pseudolayers being concentric spherical shells as indicated in the schematic (b). Centered radial drops with pure splay-type strain, as they grow, become off-centered or escaped radial-like (c), involving splay and bend, as indicated in schematic (d). (e) Enlarging drops tend toward a low-birefringence configuration, with their pseudolayers continually changing their geometry, adapting to the evolving PFCs; the texture seen here is of the transformation that is halfway through. (f) PFCs developing in a drop showing first-order birefringence. (g) Small PFC domain with its confocal parabolas in the vertical planes through the extinction brushes that appear to cross at the -1 site. (h) Drop with a central $+1$ site; other PFCs develop around it in time. Sample: C -OP5 (a); C -OP7 (c), (e)–(h). $d = 20 \mu\text{m}$ (a); $5 \mu\text{m}$ (c), (e)–(h). $T = 89^\circ\text{C}$ (a), (c), (e); 88°C (f)–(h).

Axio Imager.M1m polarizing Microscope with an AxioCam MRc5 digital camera; for controlling temperature T , an Instec HCS402 hot stage with an STC200 temperature controller (accurate to $\pm 0.1^\circ\text{C}$); for electrical studies, a Stanford Research Systems DS345 function generator connected to an FLC Electronics voltage amplifier (model A800) and a Keithley-2002 multimeter; for transmitted light-intensity measurements, a photodiode (Hamamatsu S2281) with a wideband amplifier (Hamamatsu C9329) and a PC-based digital oscilloscope (PicoScope 4262); and for measurement of static permittivity ϵ and conductivity σ , an Agilent 4284A precision LCR meter. In planar cells, the alignment direction is taken to define the reference axis x , and the direction of observation (also electric field), the axis z . Polarizer-analyzer orientation is indicated as $P(\alpha) - A(\beta)$, where α° and β° are the angles relative to x . For sine-wave (SW) or square-wave (SQW) fields, intensity, rms voltage, frequency, and period are denoted by E , U , f , and Θ , respectively.

III. RESULTS AND DISCUSSION

A. N_{TB} drops dispersed in their isotropic phase

It is useful first to recall some of the structural features of N_{TB} drops discussed in our earlier paper [27]. Figure 1 presents two of the drop geometries with which we are concerned here in the context of their electric-field-induced instabilities. The first of these is the off-centered configuration involving both splay and bend curvature strains. All the drops in Fig. 1(c), except the smallest one, are of this type, possessing shape polarity and vivid birefringence colors. These drops nucleate in the radial hedgehog (splay) geometry

[Fig. 1(a)], but as they grow, their defect cores progressively shift toward the interface. The field of twist director χ in them is rotationally symmetric about the axis through the apo- and pericenters, as in the escaped radial (ER) geometry; for this reason, although the point defect may be located slightly away from the interface, we may describe the drops as ER type. Notably, the orientation of the symmetry axis in ER drops is random in both planar and 90° twist cells, implying that it is unaffected by the aligning influence of the substrates. When the diameter D of these drops begins to exceed d , a structural transformation follows [Fig. 1(e)]. The configuration is that of low-birefringence drops, such as in Figs. 1(f)–1(h), with parabolic focal conic defects (PFCs); we may refer to these as PFC drops. Between crossed polarizers, the PFC network in a large drop displays regularly disposed extinction crosses of positive and negative types that occur alternately along a line through the defects (Fig. 2). In planform, a negative site is where the confocal parabolas cross each other and a positive site is where four parabolas meet [29,30]. In a thin sample, the positive sites are located at the substrates and the negative ones in the region of the midplane $z = 0$.

B. Flexoelectric response of N_{TB} drops in the PFC geometry

We may recall that an unstrained nematic medium is centrosymmetric and preserves its identity under inversion of its director, $\mathbf{n} \rightarrow -\mathbf{n}$. However, when it undergoes a distortion of the splay or bend type, this symmetry is lost, so that a net electric polarization develops in it. The dipole density \mathbf{P}_{sb} due to this flexoelectric (flexo-, for short) effect is given by

$$\mathbf{P}_{sb} = e_{sn}(\nabla \cdot \mathbf{n}) + e_b \mathbf{n} \times (\nabla \times \mathbf{n}), \quad (1)$$

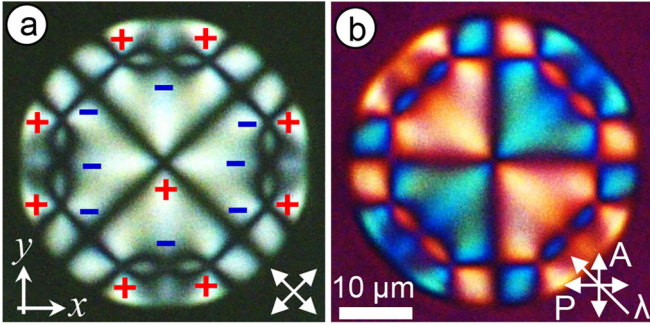


FIG. 2. A large N_{TB} drop in its PFCD geometry, formed in the isotropic liquid phase, in a 5- μm -thick layer of $C\text{-OP7}$ at 88.4°C. Plus and minus signs in (a) refer to the sense in which the extinction crosses at these PFC sites rotate relative to changing azimuth of crossed polarizers.

where e_s and e_b are, respectively, the splay and bend flexocoefficients. Flexopolarization was originally described in terms of the coupling between shape and electric polarities of molecules [31]. Its universality in anisometric quadrupolar molecules was later recognized [32]. The splay and bend distortions render the quadrupole assembly so asymmetric as to produce a nonvanishing local polarization [33]. In the N_{TB} phase, the ground state is already strained by the inherent bend distortion of the structure. The corresponding local polarization \mathbf{p} acts along the normal to the plane defined by the twist vector $\boldsymbol{\chi}$ and the director \mathbf{n} . However, due to the helical winding of vector \mathbf{p} , there exists no global polarization. A second contribution to flexopolarization, \mathbf{P}_{in} , is thought to arise [34] due to the coupling between $\boldsymbol{\chi}$ and \mathbf{n} , with

$$\mathbf{P}_{\text{in}} = -\beta_1 \boldsymbol{\chi} [\boldsymbol{\chi} \cdot \{\mathbf{n} \times (\nabla \times \mathbf{n})\}] + \beta_3 \mathbf{n} [\boldsymbol{\chi} \cdot \nabla (\mathbf{n} \cdot \boldsymbol{\chi})]. \quad (2)$$

When the helical structure is not distorted, \mathbf{P}_{in} also vanishes, so that the total flexopolarization $\mathbf{P}_{\text{f}} = \mathbf{P}_{\text{sb}} + \mathbf{P}_{\text{in}}$ remains zero. However, when an external electric field \mathbf{E} acts across $\boldsymbol{\chi}$, the latter (optical axis) rotates through a small angle in the plane normal to \mathbf{E} , just as in the flexoelectrooptic effect in cholesterics [35]; in fact, such an effect in the N_{TB} phase was previously observed and described as the electroclinic effect [15]. Reference [34] predicts a net field-induced \mathbf{P}_{in} that is accompanied by changes in both the helical angle and the wave vector.

We may now consider our observation of the inverse flexoelectric instability in N_{TB} drops dispersed in the isotropic matrix and existing in the PFCD state. While this instability in a large N_{TB} drop with multiple defect sites becomes too complex for analysis, it is found to show a regular trend in a drop with only a few defects. In Figs. 3(a) and 3(b) exemplifying this aspect, the central extinction cross represents, in planform, a negative defect site formed along the axis of two confocal parabolas that lie in the vertical xz and yz planes. The opposite dark crosses near the boundary correspond to positive defect sites. The positive defects, under excitation by a low-frequency sine-wave field, appear along x for $+E$, and along y for $-E$, their separation S being time dependent (see Video V1 in the SM [28]). In Figs. 3(c) and 3(d) showing several symmetrically disposed defects within a large N_{TB} drop, in a 20- μm -thick sample, the overall effect of the

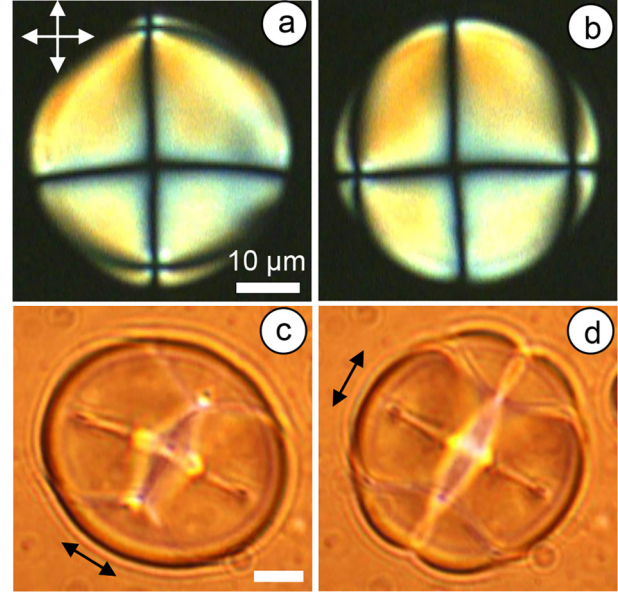


FIG. 3. (a), (b) Two frames of a time series separated by 25 s demonstrating the flexoelectric response of an N_{TB} drop in the PFCD state; 5- μm -thick $C\text{-OP7}$ layer; sine-wave field; $f = 20$ mHz, $U = 4$ V; 88°C. The drop has a negative defect site at the center; when the polarity reverses from $+U$ to $-U$, two extinction crosses, where four parabolas meet, appear at the extremities of the principal axis along y ; they move toward each other with their closest approach seen in (a); in the next polarity switch, from $-U$ to $+U$, similar extinction crosses are seen along x , while the ones along y recede and disappear from view; their closest approach is seen in (b). (c), (d). An N_{TB} drop with multiple PFC defects in a 20- μm -thick layer of $C\text{-OP5}$ with the principal axes oriented diagonally. The two frames of a time series are separated by 10 s. Sine-wave field; $f = 50$ mHz, $U = 8$ V; $T = 88^\circ\text{C}$. Double arrows indicate the direction of extension of the drop in each half of the driving cycle.

sine-wave field appears as a periodic diagonal extension of the drop, with the choice between the two diagonals governed by the polarity of E . These effects are better noticed in Video V2 of the SM [28]. The structural changes brought about by a time-varying field in a PFCD drop are also reflected in the corresponding changes in average intensity of light transmitted through the drop. Electro-optic responses of such a drop for SQW and SW excitations are illustrated in Fig. 4. In obtaining these plots, the drop was isolated from its surroundings using a pinhole screen inserted along with the analyzer that was crossed relative to the polarizer with its axis along x . Due to the high average light intensity, the signal from the transimpedance amplifier was ac coupled, with the large dc component blocked by a capacitor. The plots for SQW fields [Figs. 4(a)–4(c)] indicate small changes in optical output U_{R} following each polarity reversal. These changes occur over a time $dt \approx 0.5$ s in which structural modifications causing the movement of extinction crosses take place, and, when Θ is relatively large, the response remains nearly constant at zero after the time dt . In sine-wave fields [Figs. 4(d)–4(f)], U_{R} is close to zero around peak voltages; it fluctuates measurably around polarity switching times, i.e., in the region of low voltages in which the base state is approached before

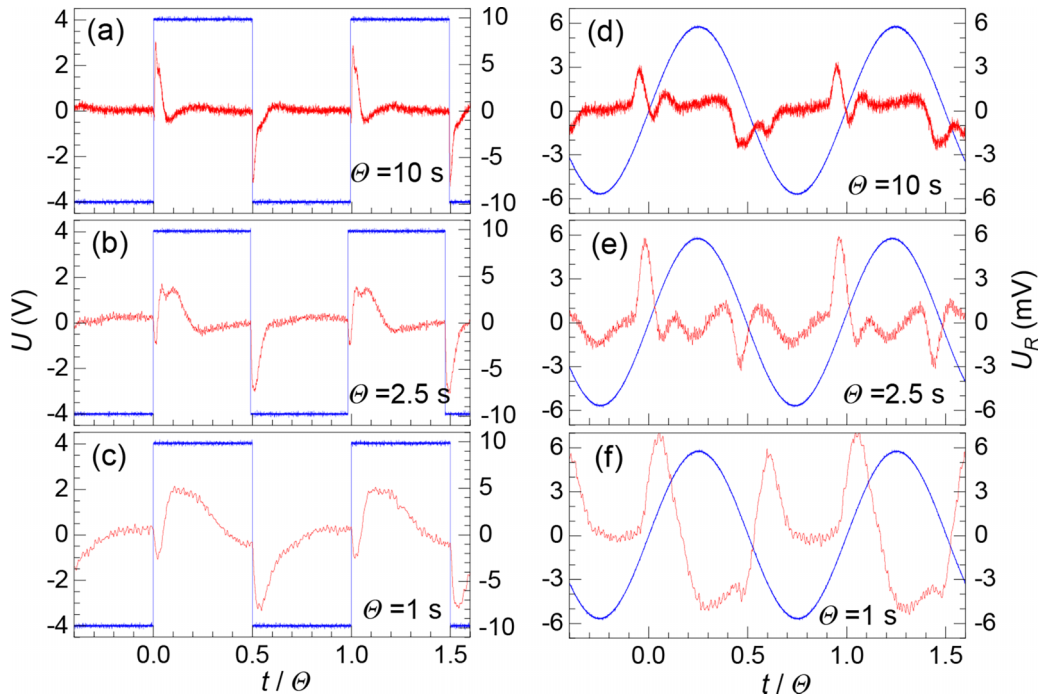


FIG. 4. Electro-optic responses of a twist-bend nematic drop, such as in Fig. 3(a), in a $5\text{-}\mu\text{m}$ -thick layer of C-OP7 at 88°C , under excitation with square-wave (a)–(c) and sine-wave (d)–(f) excitations. The response is obtained under ac coupling. Θ is the period of the electric field.

the switching, and destabilized after the switching. We may note that, in the mHz frequency regime, the bulk voltage differs from $U(t)$ both in magnitude and phase because of (a) polyimide coatings on the substrates [36], and (b) ionic effects that may include formation of intrinsic electric double layers due to selective ion adsorption [37]. The time evolution of transient electric instabilities is generally conditioned by these effects. When the PFC defects are not centered, unlike in Fig. 3, and are disposed unsymmetrically relative to the center of the drop, the flexoelectric effect manifests in varied ways depending on the initial defect state. Videos V3 and V4 of the SM [28] provide examples of this feature.

The degree of electric-field-induced distortion in a drop such as in Fig. 3(a) may be measured in terms of the separation S of the positive defects or the maximum width of the central parabola terminating at these defects. Figure 5 shows a plot of $S(U)$ to be nonlinear, approximating to a second-order polynomial. It is possible that this nonlinearity is due to the screening effect of electrical double layers that is prominent at lower voltages. Above approximately 6 V, additional defects begin to develop within the drop; at very high voltages (>14 V), as will be presently discussed, Fréedericksz instability manifests optically.

The distortion of parabolic focal conics just described is considered to be of flexoelectric origin for the following reasons. The parabolic cyclides are associated with flexoelectric polarization due to the bending of pseudolayers and associated splay distortion of the twist axes. The polarization vectors along the axis of the two confocal parabolae act oppositely. Under an electric field, to generate a net dipole moment along the field direction in a domain made mainly of a single pair of confocal parabolae, one of the parabolae narrows down, while the other opens out. To see this in some detail, we

refer to Fig. 6 (drawn after Fig. 6 of Ref. [38]), wherein the components of local polarization p_x , p_y , and p_z are indicated on the parabolic arms. In the context of second-harmonic generation in twist-bend nematics, Pardaev *et al.* [38] have previously considered a similar polarization field associated with magnetically aligned PFCs. They consider the distortion of smecticlike pseudolayers to involve, in the *absence* of any external electric field, deviation of the twist vector away from the layer normal, as in the electroclinic effect in smectic- A^* phase; this is seen to result in a net polarization with its main component *perpendicular* to the PFC axis. For the field-induced distortions at PFCs that we observe, it is

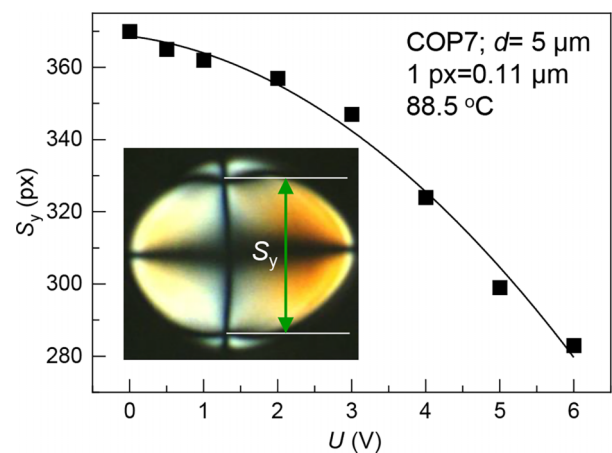


FIG. 5. Voltage variation of the maximum width S_y of the central parabola in the yz plane; inset shows the drop used for measurements; P(0)–A(90). For negative fields, the positive defects along y move outward even as similar defects appear along x .

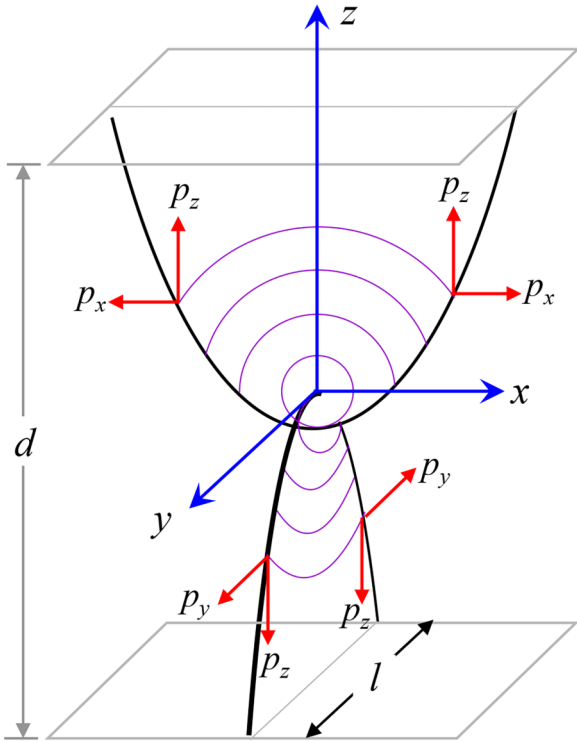


FIG. 6. Schematic of a pair of confocal parabolic line defects spanning the sample thickness. Curved lines within the parabolas represent the pseudolayer planes of equivalent phase, separated successively by the pitch of the heliconal structure. Components of local polarization p_x , p_y , and p_z are shown along the arms of the parabolas that outline the cusp regions of distorted layers.

more relevant to consider the model of flexoelectro-optic-like effect in Ref. [34]. In the region around z , the PFC axis, the applied field E , parallel to z , will have a component, E_p , perpendicular to the twist vector. Since E_p increases as we go away from z , correspondingly the contribution to p_z -via splay-bend distortions in vertical sections through z (Bouligand cuts) [35]-will also increase. When the maximum widths of the two confocal parabolas differ, a net nonzero p_z will appear in order to reduce the free energy.

As earlier noted, at higher voltages flexodeformation competes with the dielectric reorientation. The resulting time-varying textures in drops subjected to low-frequency, high-voltage, sine-wave fields, and observed with polarizers P(0)-A(90), are exemplified in Fig. 7; they are from two time-lapse series (Video V5 in the SM [28] is from one of them). At peak voltages $|U_p|$ [$t = (2n + 1)\Theta/4$; $n = 0, 1, 2, \dots$], Fréedericksz reorientation dominates and the drop is nearly homeotropic, appearing dark, as in Figs. 7(b) and 7(e). Far from $|U_p|$, on either side of $U = 0$ [$t = n\Theta/2$; $n = 0, 1, 2, \dots$], we obtain the flexoelectric patterned state that is analogous to the Bobylev-Pikin volume instability in nematics. The stripes, which involve both polar θ and azimuthal φ deviations, are observed for all settings of the polarizers; they are also seen in natural light due to the lens action from periodic out of plane tilts. The changes in the average intensity of light transmitted by an N_{TB} drop undergoing these electric instabilities are

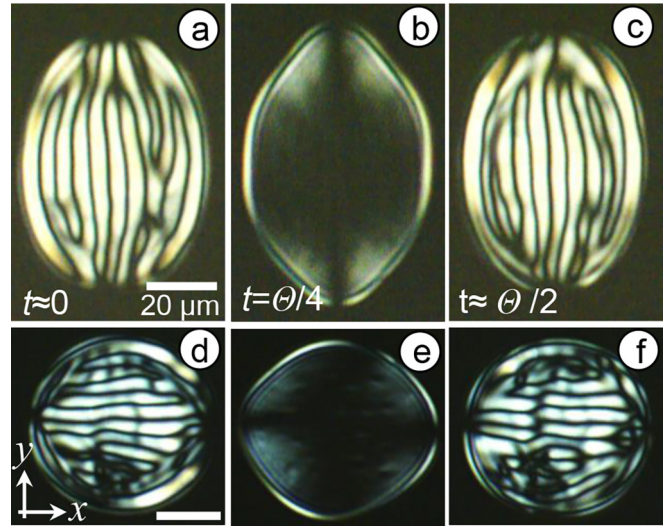


FIG. 7. Patterned flexoelectric and uniform Fréedericksz states of N_{TB} drops in a 5- μm -thick layer of C-OP7 at 88 °C. Instabilities are driven by a sine-wave field; (a)–(c) $f = 50$ MHz, $U = 15$ V; (d)–(f) $f = 40$ MHz, $U = 14$ V. White-light illumination. Under crossed polarizers P(0)-A(90), at peak applied voltages, near extinction is obtained due to the dominant dielectric torque. Striped pattern develops around zero-voltage crossings due to flexoelectric modulation, similar to the Bobylev-Pikin instability. Actually, this instability peaks shortly before and shortly after the $U = 0$ positions.

indicated in Fig. 8 in terms of $R_o(t)$, the time-varying amplified photodiode output dc coupled to a Picoscope. The dc offset of $R_o(t)$ is due to the residual light in the near-homeotropic Fréedericksz state of the drop; the two peaks in $R_o(t)$ across the polarity reversal points arise from the patterned flexoelectric states.

As earlier described, small N_{TB} drops occur in a metastable birefringent state with radial or nearly escaped radial structures, before transforming into low-birefringent drops in the incipient PFC state. Flexoelectric switching is also displayed in this precursor state as demonstrated in Figs. 9(a) and 9(b) showing the textures for opposite directions of an

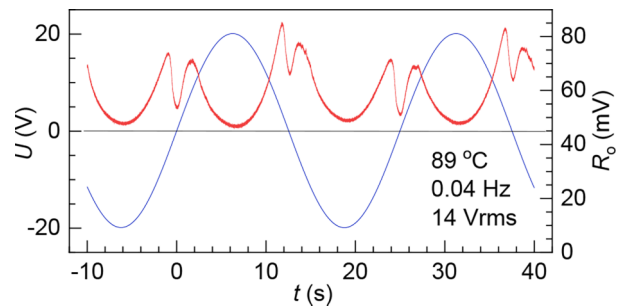


FIG. 8. Optical response R_o as a function of the applied voltage $U(t)$ in the N_{TB} drop in Fig. 7(d). Both the channels are dc coupled. The baseline of the response curve (red) is at about 45 mV. We see two R_o peaks on either side of $U = 0$ crossings, in the range 5–10 V of $|U(t)|$ due to the flexoelectric patterned instability. At peak applied voltages $|U_p|$, R_o is minimum. This corresponds to homeotropic alignment under the dominant Fréedericksz torque.

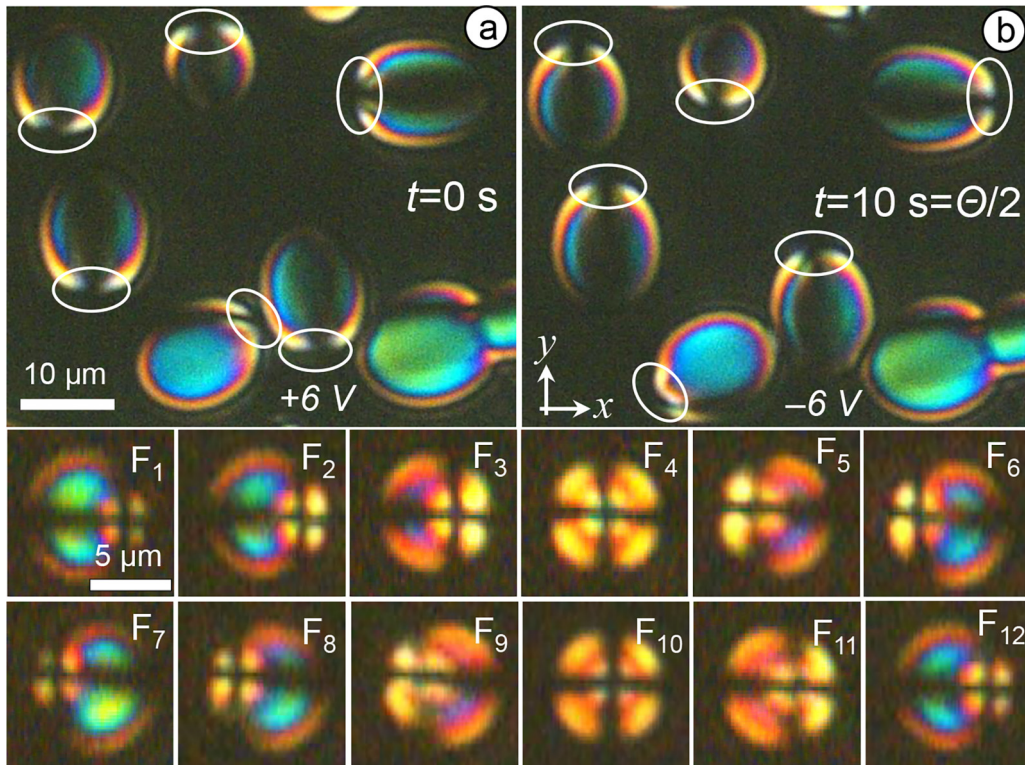


FIG. 9. (a), (b) N_{TB} drops of ER geometry in a 5- μm -thick layer of C-OP7 at 88°C for +6 V (a) and -6 V (b) of the applied square-wave field of frequency 50 mHz. Note that the extinction crosses (encircled by white lines) in all ER drops (except the composite one at bottom right) switch between opposite poles as the field polarity reverses. (F_1 – F_{12}) Successive frames of a time series showing the flexoresponse of a small N_{TB} drop exposed to a SQW field; 6 V, 5 Hz. F_1 and F_7 showing maximum interference order seem to correspond to flexodipole orientations along $\pm x$. The sequence of birefringence color change in intermediate frames suggests a rotation of the dipole vector around the y axis. Repeat period of the pattern is about 1.5 s compared to $\Theta = 0.2$ s.

applied low-frequency SQW field. The extinction cross near a pole in an elliptical drop switches to the opposite pole on field reversal. We may surmise that the flexodipoles in Figs. 9(a) and 9(b) are oppositely inclined to the layer plane, with components along the field direction. This periodic switching is found with smaller drops in bulk but not with large or composite drops (see Video V6 of the SM [28]). Even on increasing the frequency to a relatively higher value, e.g., 50 Hz, the flexoelectrically induced pattern changes are observed. They occur repetitively, but the correlation between the pattern-repeat period and Θ is lost, and more importantly, the pattern changes appear to show a rotatory motion rather than an oscillatory switching. This feature is evidenced in frames F_1 to F_{12} of Fig. 9 displaying sequentially the textures observed with a 5-Hz, 6-V SQW field during a pattern-repeat cycle; the pattern period here is 1.5 s compared to $\Theta = 0.2$ s; see Video V7 of the SM [28]. F_1 and F_7 showing maximum interference order seem to correspond to flexodipole orientations along $\pm x$. In F_4 and F_{10} , the first-order yellow birefringence color points to a predominant χ_z component of the twist director, which is possible if the defect is located close to a substrate or, equivalently, the axis of the drop is along z . Going from F_1 to F_{12} , completing the cycle, we notice the sequence of color changes suggestive of a rotation of the symmetry axis about y , such that the frames F_2 – F_6 and F_8 – F_{12} correspond to flexodipole having a nonzero component in opposite directions along z . A definitive conclusion as to whether the motion in Fig. 9

is oscillatory or rotatory requires simulation of the textures corresponding to all the possible χ fields.

C. Electrically induced drift of N_{TB} drops in the isotropic matrix

Of the various mechanisms of electrically induced transport of colloidal particles [39,40], we are concerned here with those involving motion *transverse* to the applied *ac* field. This motion may be realized through some form of field-polarity independent symmetry breaking in the induced flow patterns around the particles. For example, distortion of the director field at the site of elastic dipoles in a nematic with far-field planar alignment may be exploited to meet this requirement. This is realized in the so-called liquid-crystal enabled electrophoresis involving ion mobility and fluid-viscosity variations around dipoles formed of dispersed particles acting as radial hedgehogs and their counterhyperbolic defects; the correspondingly differing electro-osmotic fore-and-aft flow fields power the automation of dipoles [41]. Similarly, dipoles made of radial N_{TB} and hyperbolic N hedgehogs are driven to drift by forces of backflow that result from *ac* field-excited periodic flexodielectric reorientations at hyperbolic defect sites [24]. We describe below a completely different type of translatory motion of N_{TB} drops through the isotropic fluid. As we shall discuss after presenting the experiment results, it is essentially due to the loss of radial symmetry of the χ director field that enables the build-up of

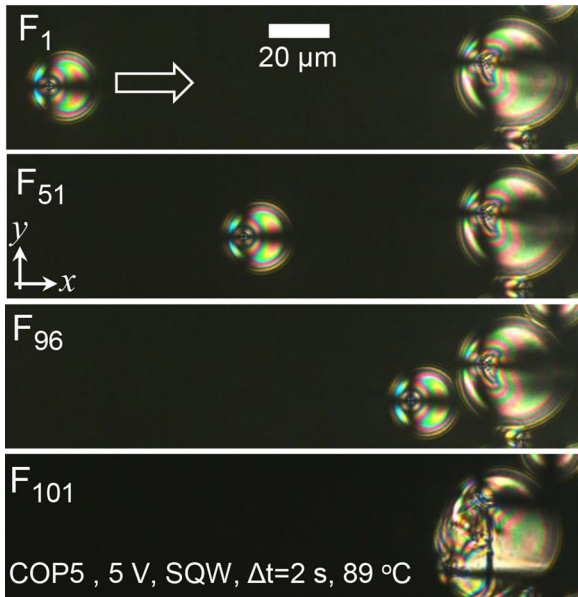


FIG. 10. (F_1 – F_{101}) Select frames F_i of a time series showing the drift of an off-centered N_{TB} drop formed in a 20- μm -thick isotropic layer of C -OP5 at 89 °C. Motion is induced by a SQW field with $U = 5$ V and f varying from 10 to 100 Hz in steps of 10 Hz after every 10 frames. Interval between successive frames $\Delta t = 2$ s. The drift decelerates exponentially with increasing f , except during the final stage before the moving drop coalesces with the larger drop at the other end, which is stationary being in contact with other drops partly seen in the frame.

an asymmetrical charge distribution and, hence, unbalanced tangential electric stresses over the drop surface.

Figure 10 illustrates the rectilinear motion of N_{TB} droplets in their ER geometry, exposed to SQW fields of frequency varying in the range 10–100 Hz, and voltage U held constant at 5 V. The frames in the figure, which are from a time series (see Video V8 of the SM [28]), show an off-centered drop of the size about the sample thickness drifting from left to right, in the direction of its apocenter, and eventually crashing

against a much larger stationary drop close to the right edge. While recording this motion, the frequency f was increased, from its initial value of 10 to 100 Hz, in steps of 10 Hz after every 10 frames. A plot of drop displacement as a function of time [Fig. 11(a)] shows that at a given f , the motion is uniform. Additionally, as seen in Fig. 11(b), the drift velocity v_x of the drop, during the first 180 s, is an exponentially decreasing function of f ; after the moving drop gets close to the larger stationary drop, it experiences a considerable acceleration. Since no elastic coupling of the drops is possible in the isotropic matrix, we conclude flexoelectric dipolar interaction as the cause of this rapid increase in speed. As previously noted, ER drops form with their symmetry axes randomly oriented in the layer plane, regardless of whether the substrates are conditioned for planar or twisted nematic alignment (see Fig. S1 in the SM [28]). Their drift direction lies along the symmetry axis, as a rule. A centered radial drop, in contrast to an ER drop, does not show any drift motion on its own; however, when it is in the path of an off-centered drifting drop, it may be kept moving along by the latter. Even when a drop is slightly off-centered, it is found to drift steadily. We may, therefore, infer the motion as rooted in the loss of spherical symmetry of the χ field. ER drops in close proximity, may come to collide, and merge, as seen in frame F_{101} of Fig. 10. More often, however, the interacting drops continue their motion along altered paths after apparent “collision;” when their approach is nearly head-on, they come to form a transient dimeric unit and start rotating about the field direction under the torque produced by noncollinear drift forces (see Fig. S2 in the SM [28]).

A distinguishing aspect of the drift motion is its occurrence over a very wide frequency range, extending from 0 Hz to 1 MHz, the upper limit up to which the study was carried out. In addition, the direction of motion is frequency determined, reversing across a critical frequency f_c on the order of charge-relaxation frequency f_r . To give a specific example, in a sample of C -OP5, we found the drift to be directed toward the apocenter below 1 kHz; but, between 1 and 10 kHz, it reversed the direction towards the pericenter.

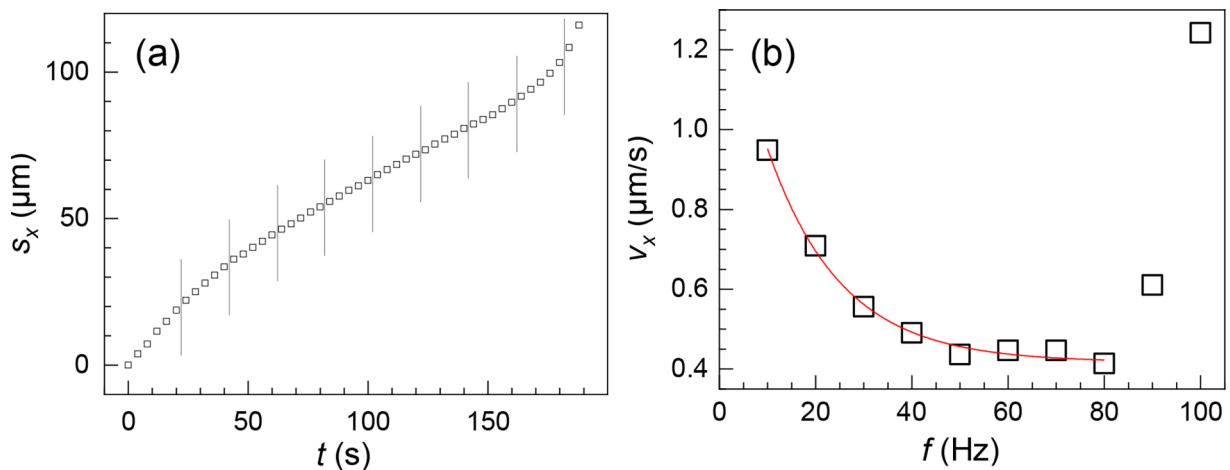


FIG. 11. (a) Displacement S_x as a function of time t for a drifting off-centered N_{TB} drop. SQW excitation; 5 V. Vertical marker lines separate regions of constant frequency, starting with 10 Hz and increasing in steps of 10 Hz after every 10 frames. The data points are for alternate frames of the time series. (b) Velocity v_x vs frequency f from the displacement-time plot on the left. Sudden rise in v_x toward the end is due to the attraction to a larger drop at the far end (see Fig. 10).

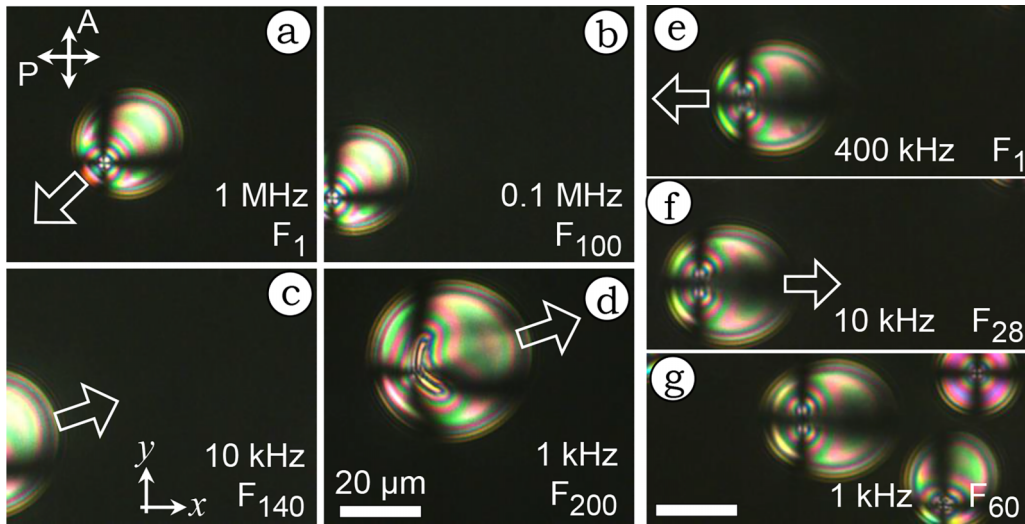


FIG. 12. (a)–(d) Select frames of a time series showing diagonal electric drift of an off-centered radial N_{TB} drop formed in a $20\text{-}\mu\text{m}$ -thick isotropic layer of $C\text{-OP5}$; planar cell, at 89.4°C . Drift direction, indicated by block arrows, is orthogonal to the electric field and along the symmetry axis of the drop, being toward the pericenter at higher frequencies, from above 10 kHz (a), (b), and toward the apocenter at frequencies at and below 10 kHz (c). F_i denotes the i th frame of the series, recorded with sine-wave fields with $U = 7\text{ V}$ and frequency f decreasing in steps from 1 MHz to 1 kHz. Heating effect at higher frequencies is evident from the reduced drop size in (a) and (b) relative to that in (c) and (d). Interval between successive frames $\Delta t = 15\text{ s}$. (e)–(g) Horizontal electric drift of an off-centered radial N_{TB} drop; frames from a time series recorded with f decreasing from 400 kHz to 1 kHz in steps; other particulars as in (a)–(d).

In Fig. 12 presenting select time images, the reversal of drift direction across 1 kHz is demonstrated for two drops, one moving diagonally, and the other axially along $\pm x$. The image series to which frames (a)–(d) of Fig. 12 belong is shown in video V9, available in the SM [28]. It may be noted that the drop appears much reduced in size at very high frequencies [Figs. 12(a) and 12(b)] compared to its size at lower frequencies [Figs. 12(c) and 12(d)]. This is mainly due to the considerable heating effect in the MHz region. Electric stresses tending to elongate the drop in the field direction at higher frequencies may also have contributed to the size reduction in a small measure. Figures 12(e)–12(g), demonstrate a similar frequency dependence of drift in a horizontally moving drop. In order to see how this frequency effect may be related to the electrical properties, we measured the electrical conductivity and permittivity of $C\text{-OP4}$ in the nematic phase, close to the N_{TB} onset temperature (We could not use $C\text{-OP5}$ for these measurements since monophasic nematic state was not obtainable with it.) The results from Fréedericksz experiments on variations of $\varepsilon(U)$ and $\sigma(U)$ in an initially planar layer of $C\text{-OP4}$ at 94°C , which are presented in Fig. S3 in the SM [28], show $\varepsilon_{\parallel} = 9.30$, $\varepsilon_{\perp} = 7.86$, $\sigma_{\parallel} = 1.05\ \mu\text{S/m}$, and $\sigma_{\perp} = 0.85\ \mu\text{S/m}$, the subscripts indicating orientation of \mathbf{n} relative to \mathbf{E} . Taking the isotropic permittivity and conductivity to be $\varepsilon_i = (\varepsilon_{\parallel} + 2\varepsilon_{\perp})/3$ and $\sigma_i = (\sigma_{\parallel} + 2\sigma_{\perp})/3$, the charge-relaxation frequency $f_r = \sigma/(2\pi\varepsilon)$ is found to be approximately 2 kHz with ε_{\parallel} and σ_{\parallel} , 1.86 kHz with ε_{\perp} and σ_{\perp} , and 2 kHz with ε_i and σ_i . The drift-reversal frequency of about 1 kHz for the drops in Fig. 12 is on the same order as these charge-relaxation frequencies.

The nature of dependence of drift velocity on field strength is perhaps the most important characteristic indicative of the mechanism underlying the motion. Figure 13 shows the drift velocity v_x , plotted as a function of U , for two N_{TB} drops

in the ER configuration, moving along x , at different field frequencies. Clearly, the velocity is a quadratic function of E . Expectedly, rate of increase of v_x at a given voltage depends on the frequency and drop size, and this is reflected in the steeper curve for 10 Hz compared to that for 100 Hz.

With the above observations on the drift motion in view, we may now discuss its possible origin. In colloidal systems, electrokinetic transport involves either the motion of particles relative to the surrounding fluid (electrophoresis) or that of the fluid relative to the particle surface (electro-osmosis). Liquid crystals generally are weak electrolytes; this is also evident from the electrical conductivity of $C\text{-OP4}$, which is on the order of 10^{-7} S/m (see Fig. S3 in the SM [28]). Hence, a dispersed particle in a mesogenic medium can acquire, e.g., by selective adsorption, a net positive or negative charge; this

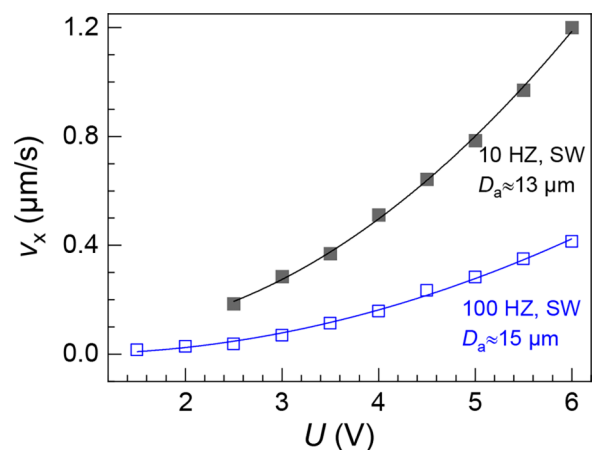


FIG. 13. Voltage variation of the drift velocity of N_{TB} drops at two frequencies; continuous lines are second-order polynomial fits.

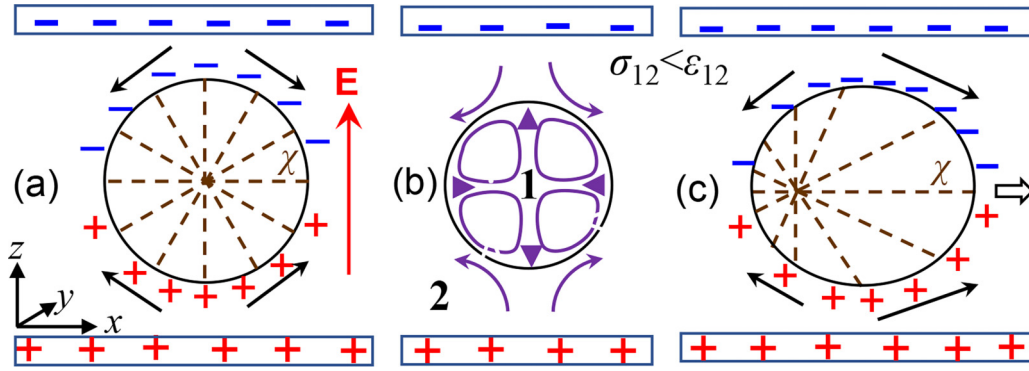


FIG. 14. Schematic of the Taylor-Melcher leaky dielectric model of EHD instability for a liquid drop immersed in another liquid. If relative permittivity $\epsilon_{12} = \epsilon_1/\epsilon_2$ and conductivity $\sigma_{12} = \sigma_1/\sigma_2$ —the individual subscripts 1 and 2 indicating, respectively, the dispersed and continuous media—the drop acquires free charges of opposite polarity over its top and bottom surfaces provided $\sigma_{12} \neq \epsilon_{12}$. When $\sigma_{12} < \epsilon_{12}$, the charges on each half and the electrode it faces are alike, as in (a). The polarities over half surfaces reverse if $\sigma_{12} > \epsilon_{12}$. Tangential stresses due to free-surface charges [indicated by sloping arrows in (a) and (c)] are balanced by toroidal fluid flows, as in (b); the flow is from pole to equator. (c) In an ER drop, the symmetrical distribution of tangential stress is lost, resulting in a drift motion of the drop.

charge, together with the neutralizing cloud of counterions it attracts, forms the electric double layer of thickness L_D , the Debye screening length; L_D , which depends on concentrations of ionic species and permittivity ϵ of the electrolyte, is typically in the range 0.1–1 μm in nematics. In response to an external field \mathbf{E} , in the so-called linear electrophoresis, a free positively (negatively) charged particle moves along (opposite to) \mathbf{E} with the steady state Smoluchowski slip velocity \mathbf{v} determined by the balance between electrical and viscous forces, and given by $v = \epsilon\epsilon_0\zeta E/\eta$, where ζ is the zeta potential or the potential drop across L_D , η is the fluid viscosity, and ϵ_0 is the free-space permittivity. Since the drift motion of N_{TB} drops takes place in a direction transverse to \mathbf{E} and with a velocity which is not linear in \mathbf{E} , it does not constitute linear electrophoresis. The E^2 growth of drop velocity implies that the motion is a type of induced-charge electrophoresis (ICEP [42]), in which charge separation at the drop surface is caused by the field itself and involves no surface charges in the absence of the field; with the induced charge density linear in E , the force on the space charges varies as E^2 . The corresponding velocity, for a dielectric particle, is given by $v = \epsilon\epsilon_0 L_D E^2/\eta$ [42,43]. Evidently, this motion would be insensitive to polarity reversals of the field and may be observed with ac excitation. The quadratic transport of the particle (or the fluid next to its surface) may take place either along [43] or transverse [41] to \mathbf{E} , depending on the space-charge distribution and properties of the fluid. When the fluid matrix is isotropic, shape anisotropy of the dispersed particles with attendant unsymmetrical charge distribution over their surface could lead to motion across a bulk field [44]. An ER drop, in effect, produces the same situation through the broken radial symmetry of its director pattern, resulting in the drift. The details of the mechanism are better visualized using the Taylor-Melcher electrohydrodynamic (EHD) approach [45,46], as detailed below, rather than the electrokinetic approach outlined above; in fact, the two approaches are unified in a recent model involving an electrical triple layer at the fluid-fluid interface [47].

The Taylor-Melcher EHD model considers the effects of a static or an oscillatory electric field on a spherical drop of one

liquid in the matrix of another immiscible liquid, assuming the two media as leaky dielectrics of differing electrical parameters, σ and ϵ [45,46]. By taking the current density to be continuous across the interface, the charge and electric stress distributions over the interface are obtained. Hydrodynamic currents are visualized such that their associated stresses balance the tangential components of electric stresses. The predicted effects regarding drop deformation and fluid flow are schematically shown in Fig. 14. The charge distributions indicated in Figs. 14(a) and 14(c) for a static field become time dependent under ac excitation. It is clear from Fig. 14(a) that when $\sigma_{12} < \epsilon_{12}$, the action of tangential stresses is to deform a spherical drop into an oblate spheroid. The deformation is ideally studied in a direction normal to the field. When viewed along the layer normal, as in this study, the circular outline of the drop should appear to increase in size when $\sigma_{12} < \epsilon_{12}$. For an off-centered N_{TB} drop having anisotropic electrical parameters, the space-charge landscape is not easy to make out. This makes the nature of electric deformation difficult to predict, with the added complexity due to the changing χ field under Fréedericksz reorientation. Despite these uncertainties, the deformation trend in Fig. 7 appears to indicate that in our case $\sigma_{12} < \epsilon_{12}$; the time images for the two drops in Fig. 7 show, for peak voltages, a greater extension along one principal axis compared to the marginal contraction along the other, with the average area showing an increase by 4–5%. Going by this result, we have schematically shown the possible charge distribution in Fig. 7(c); the corresponding left-right asymmetry in the tangential stress distribution is indicated as resulting in a net force acting toward the apocenter, along the symmetry axis; this would account for the drift observed at lower frequencies. We need to note that our measured static conductivity and permittivity values of $C\text{-OP4}$ in the nematic phase close to the N_{TB} onset temperature (see Fig. S3 in the SM [28]) show σ_{12} and ϵ_{12} corresponding to either of the principal components of the electrical parameters in the nematic phase to be very close, and their inequality reversing between parallel and perpendicular optic axial orientations relative to \mathbf{E} . These values of σ_{12} and ϵ_{12} , which pertain to the N phase, may change on going to the N_{TB}

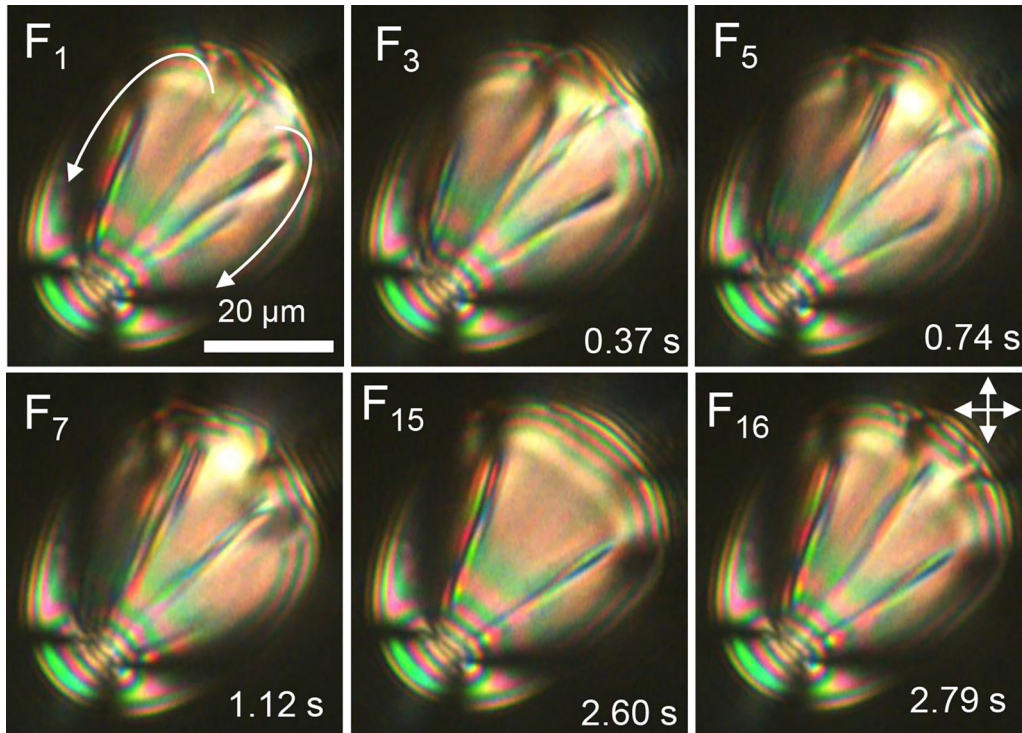


FIG. 15. Vortical flows within an ER N_{TB} drop formed in a 20- μm -thick layer of $C\text{-OP5}$; planar cell at 88 °C connected to a 15-V, 100-Hz sine-wave generator. Flows are made visible by the line defects; in frame F_1 , two outer lines are rotating as indicated by white arrow lines, while at the center a pair of line defects is developing. In F_2 , all the lines have moved further outward; the process continues with the lines moving like the hands in a butterfly swimming stroke. The drop, apparently not in translation, is actually drifting diagonally at a very low speed; this drift is seen in video V10 in the SM [28].

phase and create conditions more suitable for the drift as in Fig. 14(c).

The drop deformation in ac fields will have both steady and oscillatory parts due to the E^2 dependence [48]. In the low-frequency region, when $\sigma_{12} < \varepsilon_{12}$, the steady deformation changes the spherical drop into an oblate spheroidal one. At a critical frequency ω_c , the drop transforms back into a sphere; beyond ω_c , it turns into a prolate spheroid; ω_c is given by [49]

$$\omega_c = \sigma_2/\varepsilon_2 \sqrt{[5(\mu_{12} + 1)(\sigma_{12}^2 + 1) + (9\mu_{12} + 6)\sigma_{12} + (16 + 19\mu_{12})\varepsilon_{12}]/\sqrt{[5(\mu_{12} + 1)(\varepsilon_{12} - 1)^2]}}, \quad (3)$$

where $\mu_{12} = \mu_1/\mu_2$, the viscosity of medium 1 relative to medium 2. The coefficient of charge-relaxation frequency $\omega_2 = \sigma_2/\varepsilon_2$ is likely to be on the order of unity corresponding to the observed drift-reversal frequency (see Fig. 12).

Another important charge-separation mechanism is provided by the Carr-Helfrich model developed to account for nematic electroconvection. It relies mainly on the electrical conductivity anisotropy $\sigma_a = (\sigma_{\parallel} - \sigma_{\perp})$. When the nematic director \mathbf{n} is oblique with respect to \mathbf{E} , a transverse current develops and, in a medium with a splay-bend director wave, this leads to periodic space-charge layers of alternating polarity to exist across the wave vector, in the steady state. It is conceivable that this mechanism also plays a role in the convective flows developed within the drop.

Turning to the question of fluid flow, at lower voltages no streamlines could be discerned. On raising the field to above

0.5 V/ μm , vortical flows occurring within N_{TB} drops became clearly observable through the motion of line defects formed in the course of dielectric reorientation at the core (see Fig. S4 in the SM [28]). Figure 15 reproduces some select frames F_i of a time series recorded with $C\text{-OP5}$ subjected to a sine-wave field (100 Hz, 15 V). The circulation within the drop apparently involves two vortices outlined by the counter-rotating disclinations. The drop as a whole is also drifting diagonally at a very slow rate (0.34 $\mu\text{m/s}$). Video V10 (in the SM [28]) clearly shows the drift motion, along with the fluid circulation in the ER drop. Similar flows, with pairs of line defects sweeping around in opposite senses, are also seen in drops that are only slightly off-centered and slowly drifting (see video V11 in the SM [28]). In the classical EHD setup in Ref. [42], the fluid motion is toroidal, which is unambiguously seen in a direction perpendicular to \mathbf{E} . Seen along the field, one would expect the streamlines to appear radiating either away from or towards the center, depending on the relative values of σ_{12} and ε_{12} , and the plane of focus. The flows indicated by the in-plane rotation of disclinations in Fig. 15 are unsymmetrical and more involved.

When a small ER drop is subjected to a high field of low frequency so as to cause dynamical changes in its structure through dielectric and flexoelectric instabilities, it experiences, instead of a drift force, a torque that sets it to rotate around the field direction (Fig. 16). This rotation can be clockwise or anticlockwise depending on the asymmetry of the drop. Video V12 in the SM [28] illustrates the opposite rotation of two neighboring drops. Gyration of drops here is

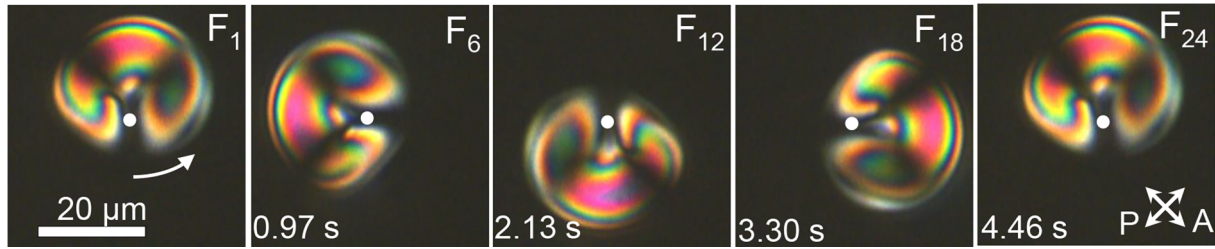


FIG. 16. An ER-type N_{TB} drop rotating about the applied field direction, with a period of 4.46 s, in a sine-wave field ($U = 14$ V and $f = 50$ Hz); 20- μ m-thick C -OP5 sample in a planar cell at 88 °C. F_i are the frame numbers of the time series with an interval of 0.194 s between successive frames. White dot marks the apparent center of rotation, where the alignment is vertical.

quite different from the Quincke rotation which occurs when the charge-relaxation time τ_1 in the drop is greater than that (τ_2) in the surrounding fluid so that the drop gets polarized antiparallel to a static field \mathbf{E} ; fluctuations in this unfavorable orientation are amplified by the electric torque to produce the rotation about any direction transverse to \mathbf{E} . By contrast, the rotation depicted in Fig. 16 is driven by oscillatory fields; also, it takes place about the field direction. It is known that complex asymmetrical shapes of particles in a colloid can lead to their nontrivial rotational and translational motions through the fluid. A study of nonlinear electrophoretic motion of polarizable particles of diverse shapes, driven by ac fields, has shown the possible symmetry-dependent trajectories [50]. The type of rotation seen in Fig. 16 is predicted in particles with a single plane of mirror symmetry and belonging to the C_s group.

IV. CONCLUSIONS

In this study, we have examined the electric-field-generated instabilities in twist-bend nematic drops dispersed in the isotropic phase, in binary mixtures of the mesogen CB7CB and 2-octadecoxypropanol. Various flexoelectric and electrokinetic responses of the drops in their ER and PFC geometries are discussed. Smaller PFC drops with a pair of confocal parabolas, when subjected to a low-frequency, low-voltage electric field acting along their common axis, undergo periodic dimensional changes so as to contribute flexoelectrically to free-energy reduction. In an ER drop, a similar result is obtained through periodic switching of the hedgehog core between opposite locations, thereby developing a component of flexodipole along the field. Sine-wave fields of

low frequency and high voltage generate Bobylev-Pikin-like patterned states at lower voltages and homeotropic alignment at peak voltages. ER drops also exhibit unusual electrohydrodynamic effects that seem to conform to the Taylor-Melcher leaky dielectric model. They occur over a very wide frequency range, extending from dc to MHz region, manifesting in the form of translatory motion of ER drops (but not centered ones in radial hedgehog geometry) along their symmetry axis, across the field direction. The direction of this motion reverses across a critical frequency close to the charge-relaxation frequency, with the drift velocity at a given frequency showing a quadratic dependence on the field strength. In high fields, vortical flows present within the ER drops are revealed by the rotational motion of radial line defects. From all these characteristics, we conclude the drift as originating in the asymmetrical induced-charge distribution over the drop surface that leads to an unbalanced tangential electric stress. Thus, the radial symmetry breaking in the off-centered drop geometry is at the root of all electrohydrodynamic effects. Analyzing the charge distribution taking the director pattern and anisotropic electrical parameters into account remains a challenge.

ACKNOWLEDGMENTS

The authors are thankful to Prof. B. L. V. Prasad for the experimental facilities, and to Prof. A. Jáklí for useful suggestions. C.V.Y. and D.S.S.R. acknowledge the financial support from the Science and Engineering Research Board (SERB), Department of Science and Technology [DST(IN)], Government of India, under Projects No. CRG/2020/001779 and No. CRG/2019/001671.

- [1] V. P. Panov, M. Nagaraj, J. K. Vij, Yu. P. Panarin, A. Kohlmeier, M. G. Tamba, R. A. Lewis, and G. H. Mehl, *Phys. Rev. Lett.* **105**, 167801 (2010).
- [2] M. Cestari, S. Diez-Berart, D. A. Dunmur, A. Ferrarini, M. R. de la Fuente, D. J. B. Jackson, D. O. Lopez, G. R. Luckhurst, M. A. Perez-Jubindo, R. M. Richardson, J. Salud, B. A. Timimi, and H. Zimmermann, *Phys. Rev. E* **84**, 031704 (2011).
- [3] I. Dozov, *Europhys. Lett.* **56**, 247 (2001).
- [4] R. Balachandran, V. P. Panov, J. K. Vij, A. Kocot, M. G. Tamba, A. Kohlmeier, and G. H. Mehl, *Liq. Cryst.* **40**, 681 (2013).
- [5] C.-J. Yun, M. R. Vengatesan, J. K. Vij, and J.-K. Song, *Appl. Phys. Lett.* **106**, 173102 (2015).
- [6] G. Babakhanova, Z. Parsouzi, S. Paladugu, H. Wang, Y. A. Nastishin, S. V. Shiyankovskii, S. Sprunt, and O. D. Lavrentovich, *Phys. Rev. E* **96**, 062704 (2017).
- [7] D. Chen, J. H. Porada, J. B. Hooper, A. Klittnick, Y. Shen, M. R. Tuchband, E. Korblova, D. Bedrov, D. M. Walba, M. A. Glaser, J. E. Maclennan, and N. A. Clark, *Proc. Natl. Acad. Sci. USA* **110**, 15931 (2013).
- [8] V. Borshch, Y.-K. Kim, J. Xiang, M. Gao, A. Jáklí, V. P. Panov, J. K. Vij, C. T. Imrie, M. G. Tamba, G. H. Mehl, and O. D. Lavrentovich, *Nat. Commun.* **4**, 2635 (2013).
- [9] D. Chen, M. Nakata, R. Shao, M. R. Tuchband, M. Shuai, U. Baumeister, W. Weissflog, D. M. Walba, M. A. Glaser,

- J. E. Maclennan, and N. A. Clark, *Phys. Rev. E* **89**, 022506 (2014).
- [10] R. R. R. de Almeida, C. Zhang, O. Parri, S. N. Sprunt, and A. Jákli, *Liq. Cryst.* **41**, 1661 (2014).
- [11] P. K. Challa, V. Borshch, O. Parri, C. T. Imrie, S. N. Sprunt, J. T. Gleeson, O. D. Lavrentovich, and A. Jákli, *Phys. Rev. E* **89**, 060501(R) (2014).
- [12] V. P. Panov, S. P. Sreenilayam, Y. P. Panarin, J. K. Vij, C. J. Welch, and G. H. Mehl, *Nano Lett.* **17**, 7515 (2017).
- [13] V. P. Panov, R. Balachandran, M. Nagaraj, J. K. Vij, M. G. Tamba, A. Kohlmeier, and G. H. Mehl, *Appl. Phys. Lett.* **99**, 261903 (2011).
- [14] V. P. Panov, R. Balachandran, J. K. Vij, M. G. Tamba, A. Kohlmeier, and G. H. Mehl, *Appl. Phys. Lett.* **101**, 234106 (2012).
- [15] C. Meyer, G. R. Luckhurst, and I. Dozov, *Phys. Rev. Lett.* **111**, 067801 (2013).
- [16] C. Meyer, *Liq. Cryst.* **43**, 2144 (2016).
- [17] A. Varanytsia and L.-C. Chien, *Sci. Rep.* **7**, 41333 (2017).
- [18] P. A. Henderson and C. T. Imrie, *Liq. Cryst.* **38**, 1407 (2011).
- [19] R. J. Mandle, E. J. Davis, C. T. Archbold, S. J. Cowling, and J. W. Goodby, *J. Mater. Chem. C* **2**, 556 (2014).
- [20] C. Meyer, D. Stoiculescu, G. R. Luckhurst, P. Davidson, and I. Dozov, *Liq. Cryst.* **44**, 232 (2017).
- [21] S. M. Salili, M. G. Tamba, S. N. Sprunt, C. Welch, G. H. Mehl, A. Jákli, and J. T. Gleeson, *Phys. Rev. Lett.* **116**, 217801 (2016).
- [22] N. Éber, Á. Buka, and K. S. Krishnamurthy, *Liq. Cryst.* **49**, 1194 (2022).
- [23] K. S. Krishnamurthy, D. S. Shankar Rao, M. B. Kanakala, C. V. Yelamaggad, and M. Kleman, *Soft Matter* **16**, 7479 (2020).
- [24] K. S. Krishnamurthy, D. S. Shankar Rao, M. B. Kanakala, and C. V. Yelamaggad, *Phys. Rev. E* **103**, 042701 (2021).
- [25] K. S. Krishnamurthy, D. S. Shankar Rao, S. Sharma, and C. V. Yelamaggad, *Phys. Rev. E* **105**, 024709 (2022).
- [26] P. Oswald, G. Poy, and K. S. Krishnamurthy, *Phys. Rev. E* **106**, 024705 (2022).
- [27] K. S. Krishnamurthy, D. S. Shankar Rao, S. Y. Khatavi, and C. V. Yelamaggad, *Phys. Rev. E* **107**, 034706 (2023).
- [28] See Supplemental Material at <http://link.aps.org/supplemental/10.1103/PhysRevE.107.044703> for video clips V1.avi to V12.avi; and SM.pdf for video clip details and phase-transition related notes.
- [29] Ch. S. Rosenblatt, R. Pindak, N. A. Clark, and R. B. Meyer, *J. Phys.* **38**, 1105 (1977).
- [30] S. A. Asher and P. S. Pershan, *J. Phys.* **40**, 161 (1979).
- [31] R. B. Meyer, *Phys. Rev. Lett.* **22**, 918 (1969).
- [32] J. Prost and J. P. Marcerou, *J. Phys. France* **38**, 315 (1977).
- [33] S. Chandrasekhar, *Liquid Crystals* (Cambridge University Press, Cambridge, England, 1992), Chap. 3.
- [34] I. Lelidis and E. Kume, *J. Mol. Liq.* **295**, 111707 (2019).
- [35] J. S. Patel and R. B. Meyer, *Phys. Rev. Lett.* **58**, 1538 (1987).
- [36] N. Éber, L. O. Palomares, P. Salamon, A. Krekhov, and Á. Buka, *Phys. Rev. E* **86**, 021702 (2012).
- [37] K. S. Krishnamurthy, *Phys. Rev. E* **89**, 052508 (2014).
- [38] S. A. Pardaev, S. M. Shamid, M. G. Tamba, C. Welch, G. H. Mehl, J. T. Gleeson, D. W. Allender, J. V. Selinger, B. Ellman, A. Jakli, and S. Sprunt, *Soft Matter* **12**, 4472 (2016).
- [39] O. D. Lavrentovich, *Soft Matter* **10**, 1264 (2014).
- [40] O. D. Lavrentovich, *Curr. Opin. Colloid Interface Sci.* **21**, 97 (2016).
- [41] I. Lazo and O. D. Lavrentovich, *Philos. Trans. R. Soc., A* **371**, 20120255 (2013).
- [42] M. Z. Bazant and T. M. Squires, *Curr. Opin. Colloid Interface Sci.* **15**, 203 (2010).
- [43] I. Lazo, C. Peng, J. Xiang, S. V. Shiyankovskii, and O. D. Lavrentovich, *Nat. Commun.* **5**, 5033 (2014).
- [44] T. M. Squires and M. Z. Basant, *J. Fluid Mech.* **560**, 65 (2006).
- [45] G. I. Taylor, *Proc. R. Soc. London, Ser. A* **291**, 159 (1966).
- [46] J. R. Melcher and G. I. Taylor, *Ann. Rev. Fluid Mech.* **1**, 111 (1969).
- [47] O. Schnitzer and E. Yariv, *J. Fluid Mech.* **773**, 1 (2015).
- [48] O. Vizika and D. A. Saville, *J. Fluid Mech.* **239**, 1 (1992).
- [49] M. S. Abbasi, R. Song, S. Cho, and J. Lee, *Micromachines* **11**, 942 (2020).
- [50] A. M. Brooks, S. Sabrina, and K. J. M. Bishop, *Proc. Natl. Acad. Sci. USA* **115**, E1090 (2018).